Electronic structure of Li with emphasis on the momentum density and the Compton profile

Helmut Bross
Arnold Sommerfeld Center, University of Munich, Germany
(Received 18 January 2005; revised manuscript received 22 April 2005; published 13 September 2005)

The electronic structure of lithium is evaluated by use of the modified augmented plane-wave method (MAPW) within the local-density and generalized gradient approximations. Due to their continuity the MAPW wave functions are especially suited for the calculation of the electronic momentum distribution function and the Compton profiles $J_{\vec{n}}(q)$ in the scattering direction $\vec{n}$ without restriction on the magnitude of the momentum. The profiles were corrected for exchange and correlation with the Lam-Platzman formulation using the self-consistent charge density and two rather sophisticated models for the momentum density function of the interacting Fermi liquid. After these corrections have been applied the theoretical spectra show good agreement with measurements along 11 different directions for momenta q ranging from 0.4 a.u. up to the biggest magnitude measured. The great wealth of experimental data allows to reconstruct the electronic momentum density with modest accuracy but yields results which only moderately well agree with the theoretical predictions.

DOI: 10.1103/PhysRevB.72.115109 PACS number(s): 71.20.Dg, 71.45.Gm, 78.70.Ck

I. INTRODUCTION

This paper was stimulated by high resolution measurements of the Compton profile (CP) along eleven directions in $\vec{q}$ space by Schülke *et al.*[1] The general trend of the profile was found in sufficient agreement with theoretical results based on Bloch functions obtained by the Korringa-Kohn-Rostocker (KKR) scheme.[2] However, at low values of the momentum q the theoretical results overestimate the profile by approximately 8% and show a pronounced cusplike behavior in the momentum range [0.5, 0.8] (atomic units) a.u. As this range is comparable with the calipers of the Fermi surface these deviations gave rise to discussions about deficiencies of the local density approximation (LDA) even when Lam-Platzman (LP) corrections[3] have been applied. The authors[1] have tried to explain these discrepancies by broadening of the occupation number near the Fermi energy. Compton-scattering investigations along the principal directions [100], [110], and [111] by Sakurai *et al.*[4] show similar deficiencies. Again, the KKR scheme improved by simple LP corrections produces broad dips located near the Fermi calipers. Using the full-potential linearized augmented plane-wave (FP-LAPW) scheme and more sophisticated LP-corrections Baruah *et al.*[5] found a quite good agreement with the experimental spectra in the momentum range up to 2 a.u., especially near the Fermi momenta. This progress is not only caused by another treatment but also by the renormalization of the experimental spectra which forces the integral over the experimental and calculated Compton profiles up to 2.0 a.u. to be equal for each principal direction. By digitalizing the spectra displayed by the authors in their Fig. 2 we have found that the KKR integral values are approximately 2%–3% bigger than the FP-LAPW values. Thus according to the Compton sum rule the LAPW scheme would overestimate the Compton profile beyond 2.0 a.u. at least by 10%.

On the background of these controversial facts a more sophisticated theoretical treatment seems appropriate. As in the previous investigation on Al (Ref. 6) the electronic structure is self-consistently calculated by use of a modification of the APW-method[7] (MAPW) in the LDA with exchange and correlation functionals which are considered to be the best at the moment.[8] As nonlocal many-body effects have occasionally been considered as being the origin of the deviations near the Fermi momenta[1] some ground state properties are calculated self-consistently within the generalized-gradient-approximation[9] (GGA) with two different forms of the functionals.[10,11]

Using two different functionals describing the momentum density function of a Fermi liquid[12,13] many body corrections of the electron momentum density (EMD) and the CP are strictly incorporated in the sense of Lam and Platzman,[3] e.g., only all-electron magnitudes have been considered. In this context it turns out to be advantageous that the MAPW scheme treats the valence and core electrons on the same footing. Furthermore the present investigation differs from the previous one in the following points: (i) The extensive information being at our disposal in the Li data[1] allows a direct comparison of the theoretical EMD with the results obtained by the Fourier reconstruction schemes.[14–16] (ii) The improper integral determining the CP in the scattering direction $\vec{n}$,

$$J_{\vec{n}}(q) = \int_{-\infty}^{\infty} \rho(\tilde{p}_x, \tilde{p}_y, \tilde{p}_z = q) d\tilde{p}_x d\tilde{p}_y, \tag{1}$$

where $\rho(\vec{p})$ is the ground state momentum density is evaluated without any truncation. Apart from the correct asymptotic behavior of the Fourier transform $\langle \vec{p} | n\vec{k} \rangle$ of the Bloch functions $|n\vec{k}\rangle$ (Ref. 17) this fact is based on a theorem on the spherical averages of EMD and CP formulated in Appendix A.

The outline of this paper is as follows: Li-specific details of the MAPW scheme as well as the results of evaluating some ground state properties are sketched in Sec. II. Section III deals with the implementation of the Lam Platzman corrections using two different functionals for the interacting

Fermi liquid. Both schemes proposed for a direct reconstruction of the EMD are briefly presented in Sec. IV. Section V is devoted to the momentum density, especially its asymptotic behavior and the comparison with the reconstruction results. The evaluation of the CPs as well as detailed comparison with the experimental data are presented in Sec. VI. Some concluding results complete the investigation.

II. ELECTRONIC STRUCTURE

A. LDA-MAPW schema

The electronic structure was self-consistently determined by use of the MAPW formalism yielding Bloch functions $\langle \vec{r} | n\vec{k} \rangle$ which due to their continuity are especially suited for the evaluation of the EMD. For details we refer to previous investigations.[6,18] All occupied electronic states are converged to 1 mRy by considering approximately 50 plane waves and five different radial functions for any value of the angular momentum $l \leqslant 2$. The density of the electrons $\rho(\vec{r})$ obtained from these states is, as consequence of the MAPW ansatz, a symmetric combination of plane waves and angular dependent contributions within the APW spheres. Because of the high symmetry inside the APW spheres it is sufficient in the case of Li to evaluate the latter contribution along four specially chosen directions[19–23] in 1/48th of the unit sphere and to construct the crystal potential in the warped muffin-tin approximation by averaging over all angular dependent contributions of these directions. In contrast to previous investigations[2] outside the APW sphere the Coulomb contribution is obtained without any further simplification whereas the exchange and correlation contributions as well as the Lam-Platzman corrections could be treated in any accuracy wanted by use of a suitably chosen fine mesh of $\vec{r}$ points. For further details see Ref. 6.

The Brillouin zone integration over the occupied states yielding the electron density, the total energy and the EMD is approximated by a sum over 728 and 3080 (5850) $\vec{k}$ points properly chosen in the irreducible wedge.[24–26] The most characteristic ground-state properties are obtained both by use of LDA and of GGA. Not only in the use of this more elaborate functional but in the warped muffin-tin approximation of the crystal potential and the continuity of the Bloch functions the present work differs from other highly accurate all-electron LDA calculations.[2,4,5] As we shall see this improved treatment is necessary to reduce the gap between theory and experiment present in the cited investigations.

B. Some ground-state properties

The total energy as a function of the unit cell volume has a pronounced minimum at 18.9900 Å^3 corresponding to the value of the lattice constant $a_0=3.3638$ Å comparable with the FP-LAPW result 3.366 Å.[10] By use of the GGA we find the slightly increased values 3.4071 Å[10] and 3.4023 Å[11] which are considerably smaller than the result 3.436 Å obtained by use of the FP-LAPW scheme.[27] We suspect that the even bigger values 3.409 and 3.471 Å recently found in LDA and GGA, respectively,[28] are due to the use of the Gaussian-linear combination of atomic orbitals (LCAO) method.

As lithium undergoes, according to recent inelastic neutron scattering experiments,[29,30] a phase transformation from bcc to a twinned 9R superstructure (Sm type) below a threshold temperature of about 78 K no experimental value of the bcc lattice constant a_0 at 0 K is available for a direct comparison. With a simple model of the thermal expansion based on the values of the lattice constant at room temperature and the coefficient of thermal expansion we have estimated the lattice constant of the instable bcc phase at low temperature to be $a_0=3.47$ Å which is quite near to the value $a_0=3.4769$ Å for the unfaulted phase at 20 K (Ref. 29) and the value $a_0=3.481$ Å quoted by Randles and Springford.[31] This still considerable deviation of 3% is common to all LDA investigations in the bcc structure, whereas in the fcc structure the deviations mostly are in the magnitude of 2% or even less. In the case of Li, the GGA produces a slightly better agreement with experiment.[28]

Values of the diameters of the Fermi body divided by the corresponding values in the case of the homogeneous electron gas of the same density denoted by the upper index 0 are listed in Table I for different values of the lattice constant approximately corresponding to $T=20$, 95, and 295 K. All quotient k_F/k_F^0 turn out to depend weakly on the lattice constant, similarly different forms of the exchange-correlation functionals have weak influence. The biggest difference occurs in the Σ direction where the LDA and GGA values differ by less than 0.3%. In accordance with other theoretical investigations[32] we find the Fermi surface slightly deviating from the spherical shape: it is a little oblate in the [100] and [111] directions and a little stretched in [110] direction. The close agreement with other investigations is demonstrated by the fourth and fifth column showing the results of a FP-LAPW (Ref. 5) calculation and an all electron self-consistent KKR bandstructure calculation[4] with the von Barth-Hedin local density approximation to the exchange and correlation functional[33] in both cases. Again the differences are in the range of some parts in thousand. A typical magnitude of the nonspherical shape is the ratio $\delta=(k_\Sigma^F-k_\Delta^F)/k_F^0$ which is found to fall in the range 4%–7% for most local theories.[1,4,31,32] With $\delta=5.9\%$ we are in accord with the result quoted by Sakurai *et al.* and quite close to the mean value of 5.4% derived from various calculations.[31] However, it should be mentioned that according to Rasolt *et al.*,[34] and explicitly demonstrated by LAPW calculations in the warped muffin-tin approximation by MacDonald[35] a nonlocal energy-dependent mass operator might considerably reduce the overall distortion of the Fermi surface to 3.7%. As consequence of the phase transformation at low temperature the experimental prognosis on the anisotropy ratio δ is analogously controversial. See for example the detailed discussions[1,36] and the results found by reconstruction of measurements of the three-dimensional electron momentum density via the direct Fourier transform method.[37]

III. LAM-PLATZMAN CORRECTIONS OF THE MOMENTUM DENSITY AND OF THE COMPTON PROFILE

A. Basic considerations

In recent investigations there has been some controversy about the significance of Lam-Platzman corrections. Sakurai

TABLE I. Free electron momentum k_F^0 and the dimensions of the Fermi surface in the principal directions as function of the lattice constant for different exchange-correlation functionals. Fourth column: theoretical values estimated from the peaks in the second derivative of the CPs by Baruah *et al.* (Ref. 5) Fifth and sixth columns: theoretical and experimental values as quoted by Sakurai *et al.* (see Ref. 4). Further abbreviations: vwn: LDA using (Ref. 8), pw91: GGA using (Ref. 10), pbe : GGA using (Ref. 11)

a[a.u.]	6.5741	6.5853	6.6337	6.6138	6.6163	Exp.
k_F^0[a.u.]	0.5929	0.5919	0.5876	0.5893	0.5892	
(vwn)	0.9774	0.9776	0.9781			
k_F^Δ/k_F^0(pw91)	0.9788	0.9789	0.9797	0.981	0.9782	0.979±0.007
(pbe)	0.9788	0.9789	0.9797			
(vwn)	1.0384	1.0380	1.0367			
k_F^Σ/k_F^0(pw91)	1.0356	1.0353	1.0341	1.037	1.0373	1.025±0.007
(pbe)	1.0358	1.0355	1.0343			
(vwn)	0.9908	0.9909	0.9911			
k_F^Λ/k_F^0(pw91)	0.9915	0.9915	0.9917	0.993	0.9916	0.995±0.007
(pbe)	0.9904	0.9904	0.9917			

et al.[4] and Tanaka *et al.*[37] mention that these corrections reduce the discrepancy between theory and experiment but that their overall effect is relatively small. However, according to Filipi and Ceperley,[38] they offer in Li a satisfactory description of the electronic correlation found by Monte Carlo (MC) calculations and bring the theoretical CP in close agreement with the experimental values.

According to Lam and Platzman[3] the value of the momentum density with correlation included and its value obtained by LDA approximation differ by

$$\Delta\rho(p) = 2\int_{V_c} \rho(\vec{r})\{N_i[\rho(\vec{r});p] - N_f[\rho(\vec{r});p]\}d^3r, \qquad (2)$$

where $N_i(\rho_0,p)$, $N_f(\rho_0,p)$ are the momentum density per electron of an interacting and a free electron gas, respectively, having the homogeneous density ρ_0. The integral extends over the unit cell and both N_i and N_f are normalized within the whole momentum space. In the spirit of LDA the all-electron charge density has to be inserted in Eq. (2). It is highly questionable whether these corrections can be split into contributions of the core and of the valence electrons even though the electron number sum rule would be satisfied when the first factor $\rho(\vec{r})$ under the integral in Eq. (2) describes either the core or valence electron charge density whereas the curly bracket is evaluated with the all-electron charge density. The use of a subcharge density in the integrand is obsolete since it completely neglects the interaction of the subsystems.

It is quite beneficial to determine the LP corrections of the Compton profile by use of the CPs of an interacting and noninteracting Fermi liquid, j_f and j_i , which are defined by

$$j_i(\rho_0,q) = 2\pi\int_q^\infty N_i(\rho_0,t)tdt \qquad (3)$$

and a corresponding equation for j_f.[39] In contrast to the momentum densities N_i and N_f both j_i and j_f are continuous at $q=p_F$. Then the LP corrections of the Compton profiles in the interacting system can be expressed by a three-dimensional integral analogous to Eq. (2),

$$\Delta J_{\vec{n}}(q) = \int_{V_c} \rho(\vec{r})\{j_i[\rho(\vec{r});q] - j_f[\rho(\vec{r});q]\}d^3r. \qquad (4)$$

To check how different functionals $N_i(\rho_0,p)$ influence the LP corrections we consider three models.

(I) The momentum density proposed by Cardwell and Cooper[40] which has been used in the recent investigation.[5] It has been derived by an analytic fit to the occupation number density of an interacting electron gas quoted by Lundqvist.[41]

(II) The momentum density function $n_f = (2\pi)^3\rho_0 N_i(\rho_0;p)$ proposed by Farid *et al.*[12] is based on very accurate results of the correlation energy of an interacting electron gas evaluated by Ceperley and Alder[42] by use of a quantum Monte Carlo (QMC) method and allows a parameterization by four quantities μ_0, μ_1, ν_0, and ν_1 . For any value of the density ρ_0 we have evaluated μ_0, μ_1, ν_1 from the listed values by use of spline interpolation whereas ν_0 is determined by the normalization requirement.

(III) Following Barbiellini and Bansil[43] we consider the parameterization

$$N_i(\rho_0;p) = A_1 + A_2x^2 \quad \forall \quad 0 \leqslant x \leqslant 1 \qquad (5)$$

$$= A_3\exp[-A_4(x-1)] + T/x^8 \quad \forall \quad x \geqslant 1, \qquad (6)$$

where $x=p/p_F$ with $p_F=(9/4\pi)^{1/3}/r_s$ and $r_s=(3/4\pi\rho_0)^{1/3}$. The parameters A_1 and A_2 just as the quasiparticle renormalization factor at the Fermi surface Z_F are obtained by a least squares fit to the QMC data of Ortiz and Ballone.[13] According to Yasuhara and Kawazoe[44] the coefficient T is expressed by the pair correlation function at $r=0$, which has been obtained analytically by Overhauser[45] and distinctly differs from the values quoted by Farid *et al.*[12] The coefficient A_3 is defined by the renormalization factor $A_3=A_1+A_2-T-Z_F$

TABLE II. Optimal fit parameters of model III and the quasiparticle renormalization factor of models I and II. All in atomic units.

	$r_s=0$	$r_s=1$	$r_s=3$	$r_s=5$	$r_s=7$	$r_s=10$
A_1	1.0000	0.9984	0.9820	0.9802	0.9778	0.9080
A_2	0.0000	−0.0360	−0.0913	−0.1671	−0.2379	−0.2337
A_4	4.4836	3.3401	3.1302	3.6508	3.0666	2.4714
Z_F(III)	1.0000	0.9451	0.8425	0.7204	0.6421	0.5774
Z_F(I)	1.0000	0.9048	0.7144	0.5240	0.3336	0.0480
Z_F(II)	1.0000	0.8592	0.7000	0.6025	0.5319	0.4540

whereas the parameter A_4 is fixed by the electron number sum rule yielding the nonlinear equation

$$(A_4^2+2A_4+2)/A_4^3=[(1-A_1)/3-A_2/5-T/5)/A3. \quad (7)$$

By this choice of the parameters we obtain a close fit to the many-body data. Values of the parameters A_1, A_2, A_4, and Z_F are given in Table II for different values of r_s.[56]

From Table II we learn that the values of Z_F are significantly different in the three models. In addition they show a quite different decay at large values of p. The tail of model III is farther reaching than in model II whereas in model I $N_i(\rho_0,p)$ vanishes beyond $p\approx 1.51(3\pi^2\rho_0)^{1/3}$.

B. Explicit calculations

The way how the LP corrections are evaluated in previous investigations is hard to be judged. Sakurai *et al.*[4] give no details at all whereas Baruah *et al.*[5] used their self-consistent charge density in the muffin-tin spheres but assumed the density to be flat with little structure in the interstitial region.

In the present investigations the nonshape restricted charge density obtained from the self-consistent MAPW calculations is used without any truncation. For further details we refer to the preceding investigation[6] where, in addition explicit expressions for the Compton profile $j_i(\rho_0,q)$ of the interacting Fermi liquid described by the momentum density of models I and II are given.

The results obtained are summarized in Fig. 1 showing the corrections of the momentum density $\Delta\rho$ in the upper panel and the corrections of the Compton profile ΔJ in the lower panel. For completeness many body corrections of the momentum density obtained by QMC calculations are shown, too. In the low momentum regime they are close to the results obtained with model I but favor the parameterization of model II for $q>0.5$ a.u. It is common to all models that the correction of the momentum density has an accelerated increase in the low momentum region and a rapid variations around the value $q_0\approx 0.608$ a.u. as a consequence of the discontinuity of the functions $[N_i(\rho_0;)-N_f(\rho_0;p)]$ for the homogeneous electron gas. At bigger values of q model III has the weakest decay followed by model II whereas the range in model I is rather limited. The shape of of the density curves is quite similar but their magnitudes differ by the factors ≈ 0.6 and ≈ 0.3, in the case of models I and III, respectively, from the result of the Farid *et al.* parameterization. Due to the two-dimensional integration the corrections of the Compton profile vary smoother but still have a spike near q_0. On the low momentum side both models I and III approach the same value −0.0434 a.u. which is to be compared with the values −0.0567 a.u. obtained by model II. On the high momentum side the three models differ from another by their decay: again model III has the farthest range. The height of the spike is almost comparable in models I and II whereas it is by a factor 0.58 smaller in model III thus guaranteeing the validity of the electron number sum rule. These results demonstrate that different parameterizations of $\{N_i[\rho(\vec{r});p]-N_f[\rho(\vec{r});p]\}$ essentially influence the CP profiles especially near the Fermi break p_F given in Sec. II B. To complete this analysis results obtained with the spherical charge density and the constant charge density between the APW-spheres derived by Moruzzi *et al.*[46] in the KKR scheme are also listed in Table II which give an idea of the LP corrections in the previous investigations.[4] They have the peculiarity that the critical momentum q_0 occurs at 0.622 a.u. and that the magnitude of the corresponding curves are reduced by the overall factor ≈ 0.8 with the consequence that they have less influence on the CP corrections near p_F. As we

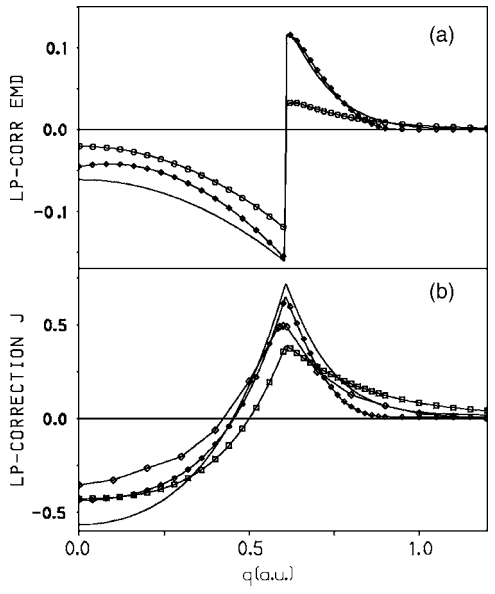

FIG. 1. Lam-Platzman corrections (a) of the momentum density, (b) the Compton profile. Full-line: MAPW-II, chain of diamonds: MAPW-I, chain of circles: MAPW-III, chain of squares: MC result (see Ref. 38). The momentum density in electrons/a.u.^{3}, and the Compton profile in 0.1 electrons/a.u.

shall see in the following the MAPW charge density together with parameterization by Farid *et al.* result in the good agreement of the CPs with the experimental results. We suppose that the LP corrections obtained by Baruah *et al.*[5] behave quite similarly but that their magnitude is reduced by 30%, as a consequence of the Cardwell-Cooper momentum function.

IV. RECONSTRUCTION METHODS

Different methods have been proposed to reconstruct the three-dimensional momentum distribution directly from the experimental data. For details we refer to the review article by Mijnarends.[14] In this section we will not only apply the Fourier-Hankel method[14,15] and the Fourier-Bessel method[16] to the measurements[1] but also prepare the basis for the comparison with the theoretical results presented in the following sections.

In the case of a crystal belonging to the cubic group O_h the first method is based on the expansion of the EMD in Kubic harmonics (KH),

$$\rho(\vec{p}) = \sum_L \rho_L(p) K_L(\vec{p}^0). \tag{8}$$

The index L stands for a pair (l,s), where s counts the various KH for a specific value of l. By use of an orthogonal transformation α defined by

$$\boldsymbol{\alpha} \cdot \vec{n} = (0,0,1) \tag{9}$$

which carries from the original cubic axis to the new coordinate frame $\tilde{p}_x$, $\tilde{p}_y$, $\tilde{p}_z$ with the $\tilde{p}_z$ axis in the scattering direction $\vec{n}$ the Compton profile is given by the sum of products over L

$$J_{\vec{n}}(q) = 2\pi \sum_L F_{\vec{n},L} g_L(q). \tag{10}$$

In spherical coordinates ϑ, ϕ with polar axis in $\vec{n}$ the first factor is defined by the azimuthal integral

$$\frac{1}{2\pi} \int_0^{2\pi} K_L(\boldsymbol{\alpha}^{-1} \cdot \vec{p}^0) d\phi = F_{\vec{n},L} P_l(\cos\vartheta)$$

$$\forall -1 \leqslant \cos\vartheta \leqslant 1, \tag{11}$$

where P_l denotes the Legendre polynomial of degree l. It only depends on the unit vector $\vec{n}$. In contrast the second factor defined by

$$g_L(q) = \int_q^\infty \rho_L(t) P_l\left(\frac{q}{t}\right) t dt \tag{12}$$

contains all information about the momentum density. In Sec. VI we will use Eq. (10) for a direct evaluation of the CPs along a certain direction. See Fig. 9. It is less time consuming than the usual two-dimensional integration according to Eq. (1) as it only needs the expansion coefficients ρ_L which can be found by a least-squares fit.

The reconstruction procedure is based on the assumption that a small number of $g_L(q)$ is sufficient to adequately describe the profiles which may be determined by a least-squares fit based on Eq. (10). For this and the Fourier-Bessel reconstruction scheme it is advantageous that due to the optimal choice of the directions by Schülke *et al.*[1] with the weights $g_{\vec{n}}$ listed in Table 3 (see Ref. 57) the matrix determining the corresponding normal equations has dominant diagonal elements. Nevertheless, at most the first four functions $g_L(q)$ can be considered to be reliable. Finally, the expansion coefficients $\rho_L(p)$ are obtained by solving the Volterra equation (12) as described by Mijnarends.[14]

The central magnitude of the Fourier-Bessel[16] method is the reciprocal form factor $B(\vec{r})$,[47] which is the three-dimensional Fourier transform of $\rho(\vec{p})$,

$$B(\vec{r}) = \int_\infty \rho(\vec{p}) \exp(i\vec{p} \cdot \vec{r}) d^3\vec{p}. \tag{13}$$

In the coordinate system $\tilde{p}_x \tilde{p}_y \tilde{p}_z$ we get

$$B(r\vec{n}) = \tilde{B}(0,0,r) = \int_{-\infty}^{\infty} J_{\vec{n}}(p) \exp(ipr) dp \quad \forall \quad -\infty \leqslant r \leqslant \infty, \tag{14}$$

when $\tilde{r} = r\tilde{n}$ is chosen. The reciprocal form factor along a given direction $\vec{n}$ is completely determined by the one-dimensional Fourier transform of the CP on this direction. Rapid variation of $J_{\vec{n}}$ essentially influence the asymptotic behavior of B which is expected to be rather orientation dependent in the case of Li. Usually, the reconstruction takes place in two steps:[1] (i) as $B(\vec{r})$ is invariant under all operations of the cubic group it can be expanded in a series of KHs where the expansion coefficients $B_L(r)$ are again obtained by a least-squares fit using the set of the $B(r\vec{n})$'s $\forall 0 \leqslant r \leqslant \infty$. (ii) The inverse Fourier transform provides the expansion coefficients of the EMD

$$\rho_L(p) = \frac{(-i)^l}{2\pi^2} \int_0^\infty B_L(r) j_l(pr) r^2 dr, \tag{15}$$

where j_l denote the spherical Bessel functions of first kind. In accord with the remark in Sec. III A all-electron profiles of lithium are obtained by adding the contribution of the 1s profile according to Biggs *et al.*[48] To avoid ambiguities the CPs beyond 3.0 a.u. are augmented up to 160.0 a.u. by the Li atomic profile joining smoothly the profile at 3.0 a.u. The reconstructed momentum density at a certain value of $\vec{p}$ essentially depends on the convergence of Eq. (8). Since each $p^l K_L(\vec{p}^0)$ is an homogeneous polynomial of order l in the components of $\vec{p}$ the least-squares fit of $B(r\vec{n})$ must be restricted to low values of l. To obtain a more reliable result for the reconstructed $\rho(\vec{p})$ the experimental information may be enlarged by an increase of the number of scattering directions. Different from Tanaka *et al.*[49] who had mapped out the values of $B(\vec{r})$ on a cubic mesh of $\vec{r}$ points by interpolation we have determined directly the $B(r\vec{n})$ along 24 specifically chosen directions by a two-dimensional interpolation from the 11 experimental Bs. For details we refer to Appendix C. Based on this information for any value of $\vec{p}$ the momentum density is given by the inverse Fourier transform

$$\rho(\vec{p}) = \frac{1}{8\pi^3}\sum_{j=1}^{24} g_j \int_0^\infty B(r\vec{n}_j)\sum_s \cos[(\vec{p}_s\cdot\vec{n}_j)r]r^2 dr. \quad (16)$$

Here the second sum goes over the elements of the star of $\vec{p}$. In the following sections we shall compare the expansion coefficients for $l=0$, 4, 6, and 8 obtained with either reconstruction schemes with the corresponding MAPW predictions.

V. ELECTRON MOMENTUM DENSITY

A. Basic equations

In the one-particle approximation the electron momentum density is defined by the sum

$$\rho(\vec{p}) = 2\sum_{n\vec{k}} |\langle\vec{p}|n\vec{k}\rangle|^2 f_{n\vec{k}} \quad (17)$$

extended over the first Brillouin zone and over occupied bands. The preceding factor 2 is due to the spin degeneracy. $f_{n\vec{k}}$ denotes the Fermi-Dirac distribution function. Provided the Fourier transform of the Bloch functions is defined by

$$\langle\vec{p}|n\vec{k}\rangle = \frac{1}{(2\pi)^{3/2}}\int_{V_c} \exp(-i\vec{p}\cdot\vec{r})\langle\vec{r}|n\vec{k}\rangle d^3r, \quad (18)$$

where V_c denotes the volume of the elementary cell, the integral of momentum density over the momentum space gives the number of electrons within the unit cell.

$$\int_\infty \rho(\vec{p})d^3p = 2\sum_{n\vec{k}} f_{n\vec{k}}. \quad (19)$$

As usual the Bloch function $\langle\vec{r}|n\vec{k}\rangle$ is normalized within the elementary cell. The Fourier transform is only nonzero provided $\vec{p}$ coincides with $\vec{k}$ modulo a reciprocal lattice vector $\vec{K}$,

$$\langle\vec{p}|n\vec{k}\rangle = \delta_{\vec{p},\vec{k}+\vec{K}}\frac{1}{(2\pi)^{3/2}}\int_{V_0} \exp(-i\vec{p}\cdot\vec{r})\langle\vec{r}|n\vec{k}\rangle d^3r, \quad (20)$$

as a consequence of the Bloch theorem. In the following it will turn out to be quite advantageous that the Fourier transform of the MAPW functions approaches zero as $1/p^4$ for large values of $|\vec{p}|$ (cf. Ref. 26) as a benefit of their continuity on the APW sphere. In this respect the MAPW scheme is superior to other schemes used for example in the investigations[2,4,5,37] which show a weaker decay caused by the discontinuity of the wave functions and of their first derivatives. Explicit expressions for the Fourier transform given in Ref. 26 are quite adequate for numerical calculations based on MAPW results.

B. The momentum density along crystallographic directions of high symmetry

Figure 2 shows the EMD along the three principal directions in the interval $0\leqslant p\leqslant 1.5$ a.u. These curves have been obtained from MAPW results where for each value of $\vec{p}$ a Bloch vector $\vec{k}$ within the first Brillouin zone is found by

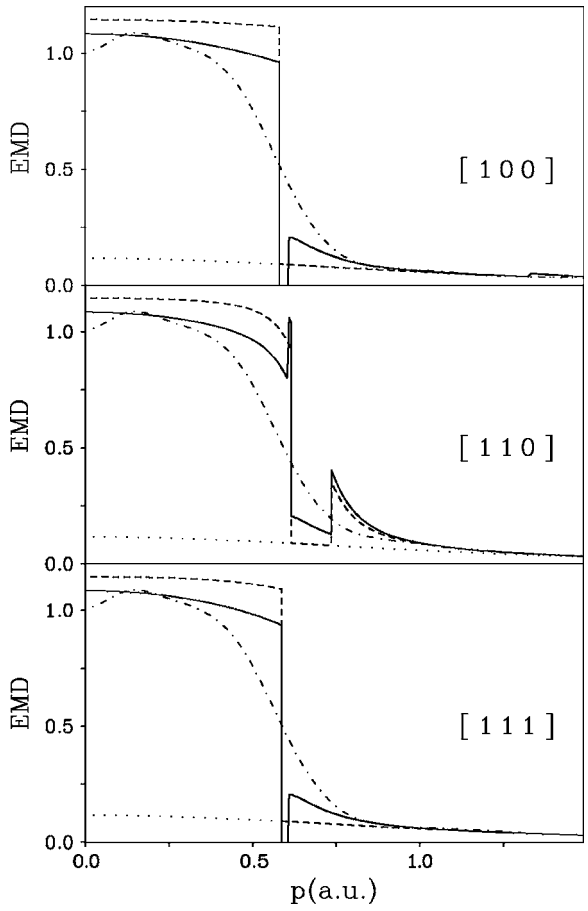

FIG. 2. Unfolded electron momentum density of Li along the [100], [110], and [111] directions. Dashed curve: All electron LDA results, full curve: LP corrections included, lower dotted curve: core contribution, dashed-dotted curve: Fourier-Bessel reconstructed experimental result (see Ref. 1) according Eq. (16). Details are explained in the text. The momentum density in electrons/a.u.[3]

subtracting a suitably chosen reciprocal lattice vector $\vec{K}$, e.g., $\vec{p}=\vec{k}+\vec{K}$. This and most of the following results are only derived within LDA and for the lattice parameter $a=6.57408$ a.u. ≈ 3.479 Å. Dotted curves show the all-electron results in the noninteracting picture whereas the dashed curves denote the contribution from the $1s$ electrons which is almost isotropic. In the interval $0\leqslant p\leqslant 0.615$ a.u. the contributions of the valence electrons are dominant with a discontinuity corresponding to the Fermi surface calipers listed in Table I. As a consequence of the periodicity of $f_{n,\vec{k}}$ in the extended zone scheme these discontinuities are more or less strongly repeated at higher values of p. Especially, a pronounced dip occurs at $p=0.759$ a.u. along the [110] direction due to the secondary Fermi surface centered at $\vec{K}_{110}$. On the low momentum side the contribution of the valence electrons show an orientation dependent decrease. Beyond the discontinuities the contribution due to the rapid variation of the valence Bloch functions near the nuclei asymptotically merges with the core electron contribution. Lam-Platzman corrections are included in the full curves using the momentum density function for an interacting Fermi liquid proposed by Farid *et al.*[12] In agreement with Fig. 1 they reduce the

EMD on the low-momentum side by up to 16%. In the interval [0.603,0.614] a.u. they undergo a drastic increase from −0.160 to 0.116 a.u. and a rapid decay at higher values of p. The interplay of this variation with the Fermi edge singularities produces particular features in the EMD which are strongly orientation dependent but which need not to be taken too seriously as they are a consequence of the isotropy of the LP corrections.

The momentum density obtained by use of the Fourier-Bessel scheme after having added the $1s$-core profile according to Biggs[48] to the experimental data[1] using Eq. (16) are also displayed by the dashed-dotted curve. Over the whole momentum range the reconstructed momentum density turns out to be quite smooth without any sign of a dip near p_F. The agreement with the theoretical predictions is quite poor. Apart from many-body effects these differences are to the momentum-space resolution of the experiment which is enforced by the reconstruction scheme. The dip of the reconstructed momentum density near $q=0$ is hard to understand and causes some doubts about the accuracy of the experimental CPs for small values of q. As we shall see in the next subsections the Fourier-Hankel scheme produces a even poorer agreement.

C. The spherically averaged momentum density and Compton profile

Provided the momentum density $\rho(\vec{p})$ only depends on the absolute value of $\vec{p}$ the two-dimensional integral Eq. (1) over the whole plane in $\vec{p}$ space with normal $\vec{n}$ in scattering direction and with distance q from the origin is

$$J(q) = 2\pi \int_q^\infty \rho(p) p dp, \tag{21}$$

independent from the orientation of $\vec{n}$. Thus we alternatively have

$$\rho(p) = -\frac{1}{2\pi p}\frac{dJ(p)}{dp} \quad p \neq 0 \text{ and} \tag{22}$$

$$\rho(0) = -\frac{1}{2\pi}\frac{d^2J(p)}{dp^2}. \tag{23}$$

(For details see the monograph.[14])

Both relations have been used in the case of gases, liquids, and polycrystalline solids. However, they still remain valid if either the CP or the EMD are spherically averaged. (See Appendix A.) For example Ohata *et al.*[50] used the spherical average obtained from the profiles along the three principal directions to reconstruct the spherical average of the EMD of Al according to Eq. (21). A far more accurate average is to be expected from the CPs measured along 11 different directions nonuniformly distributed in the irreducible wedge by Schülke *et al.* in the case of Li. On the theoretical side the reverse procedure is quite promising: Evaluate the EMD along specifically chosen directions which are well suited for the orientational averaging and derive the spherical average by use of the one-dimensional integral Eq. (21). As we shall see in the following section this way is considerably less computationally expensive than the evaluation of the CPs by performing the two-dimensional integrals according to Eq. (1) and thus allows one to cover a wider range of momenta q. In the following, the results of both strategies are compared. We have used 24 specially chosen directions in the irreducible wedge of the Brillouin zone (BZ) which have been obtained by requiring that the first 68 Kubic harmonics $K_L(\vec{p}^0)$, e.g., $L<52$, have nonvanishing residua in the sense as required by Bansil[19] and others.[20–23] Again the EMDs in the noninteracting picture are discontinuous at the corresponding Fermi diameter. Apart from this small region each EMD behaves quite similar to the nearest EMD displayed in Fig. 2. Especially, the directions within a cone of solid angle 0.12 along the [110] direction have EMDs with pronounced dips beyond 0.736 a.u. The spherical average of the EMD obtained from the results along these directions is displayed in Fig. 3. It is superimposed by the LP corrections which are quite weak beyond 1.0 a.u. It is quite conceivable how larger sets of special orientations would further smooth the decay. The low hump at higher values of p originates from the Fermi singularities in the second zone BZ. In addition the spherical average of the EMD obtained by applying the reconstruction schemes of Sec. IV to the experimental data[1] are also displayed. Apart from the low momentum region they almost coincide, but distinctly differ from the theoretical result up to $p=1.0$ a.u. Beyond this value they asymptotically merges with core contributions. Figure 4 shows the orientational dependence of the EMD described by the first expansion coefficients $\rho_L(p)$, $L>0$ and their comparison with the result of the reconstruction schemes. The first peak in the range [0.585,0.620] a.u. manifest the strong variation of the momentum density near Fermi surface diameters, the additional peak near 0.736 a.u. reflects the periodicity of $f_{n,\vec{k}}$ in the extended zone scheme. From these results we learn that the basic assumption of the Fourier-Hankel scheme is poorly fulfilled as it is not sufficient to approximate the orientational dependence of the EMD by a small number of Kubic harmonics. The disagreement with the theoretical results clearly visible in Fig. 4 is fully plausible. As mentioned before the discontinuities at the Fermi energy especially influence the asymptotic behavior of the reciprocal form factor B but do not cast into doubt its expansion in KHs. Therefore, it is hard to understand why

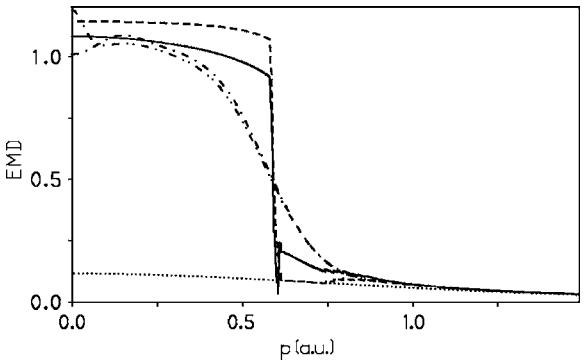

FIG. 3. Orientation-averaged value of the EMD. Dashed dotted line: Fourier-Bessel, dashed double-dotted line: Fourier-Hankel reconstruction scheme. For further details see Fig. 2.

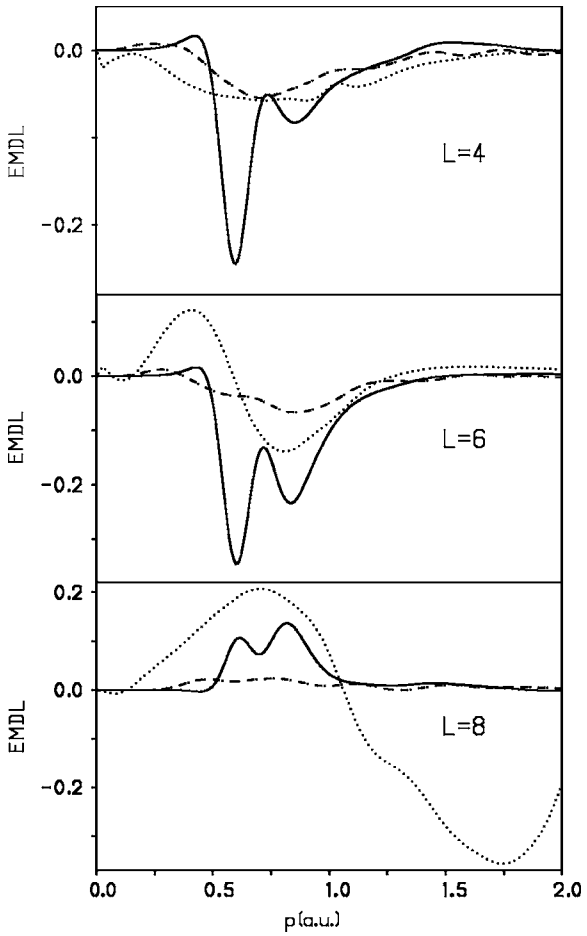

FIG. 4. Expansion of the EMD in terms of KH normalized to 4π on the unit sphere (see Ref. 51). Full line: MAPW results folded with a Gaussian of 0.14 a.u. full width at half maximum (FWHM) to take into account the experimental momentum resolution, dashed dotted line: Fourier-Bessel result, dashed dotted line: Fourier-Hankel result. In units 0.1 electrons/a.u.[3]

the Fourier-Bessel curves, especially for $l=6$ and $l=8$, only qualitatively follow the shape of theoretical curves. Figure 5 shows the spherically averaged EMD in a semilogarithmic scale. In accordance with general considerations on the continuity of the MAPW-functions we find a decay by 12 orders of magnitude in the momentum range up to 65 a.u. confirming that the MAPW Fourier transform $\langle \vec{p}|n\vec{k}\rangle$ is well suited for evaluation of Compton profiles. On this scale the contributions to the EMD from all electrons and from the 1*s* core electron are hardly distinguishable beyond $p=1.0$ a.u. It is remarkable that the momentum density in LDA obtained from the self-consistent field (SCF)-MAPW density by use of

$$\rho(p) = 2\int_{V_c} \rho(\vec{r}) N_i[\rho(\vec{r};p)] d^3r \tag{24}$$

and the all-electron spherical EMD almost merge up to $p=7.5$ a.u. At large values of p this quantity is obviously underestimated in LDA. Globally, the orientational dependence of the EMD is described by its variance $\sigma(p)$, the

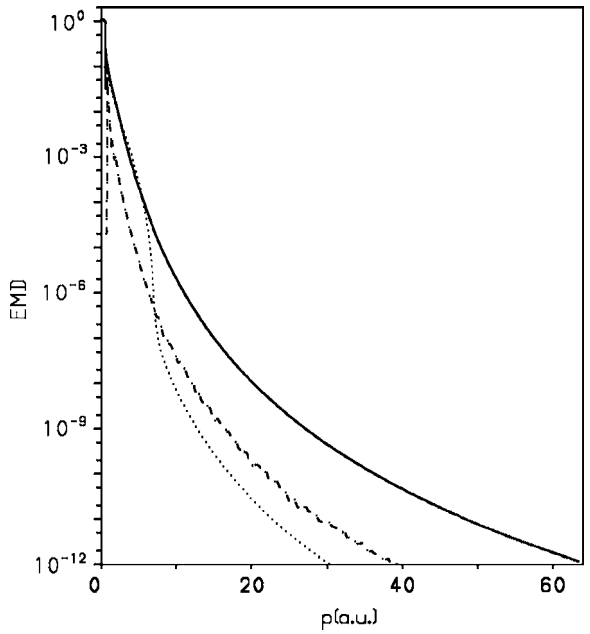

FIG. 5. Spherical average of the all electron momentum density of Li on a semilogarithmic scale (full curve). Dashed dotted curve: variance of the CPs, dotted curve: momentum density in LDA using Eq. (24). Momentum densities in electrons/a.u.[3]

square root of the squared deviations of $\rho(\vec{p})$ from its mean value $\rho_{\mathrm{av}}(p)$ averaged over the unit sphere. In the semilogarithmic plot of Fig. 5 it is displayed for $p>0.8$ a.u. by the dashed-dotted curve. Is is quite large at the low momentum side as consequence of the Fermi-edge singularities but becomes negligible beyond a moderate value of p where the contribution from the core region is dominant. Anticipating the considerations of the next section we have evaluated the average value of the CP via Eq. (21). According to Fig. 6 it decays by nine orders of magnitude in the momentum range up to 65 a.u. With regard to this result we have great doubts whether extending the integration over the momenta to about 5.0 a.u. gives an accuracy of 10^{-4} as claimed by Ohata *et*

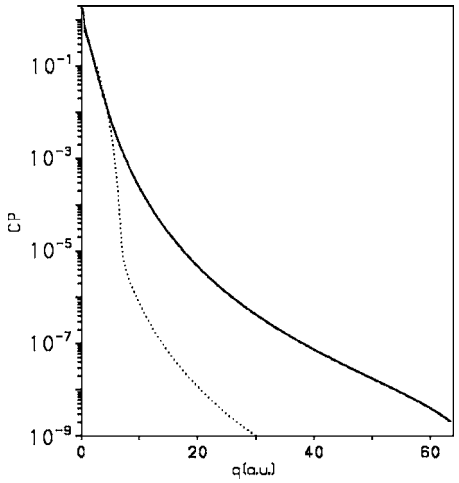

FIG. 6. Spherical average of the the Compton profile Li on a semilogarithmic scale (full line). Dotted curve: CP in LDA using an analogous relation to Eq. (24). Compton profile in electrons/a.u.

al.[50] since the KKR Fourier transform used by these authors certainly does not show a more rapid decay.

VI. COMPTON PROFILE

A. Evaluation of two-dimensional integrals

In the so-called impulse approximation the Compton profile is defined by the two-dimensional integral over the whole plane in $\vec{p}$ space with the normal $\vec{n}$ in the scattering direction according to Eq. (1). A Cartesian coordinate system is introduced with the $\tilde{p}_z$ axis along the direction $\vec{n}$. The considerations of the of the previous section allow a sophisticated treatment of the improper integral defining $J_{\vec{n}}(q)$. According Fig. 5 the orientational dependence of the momentum density can be neglected beyond $P_{\max}=8.0$ a.u. with an accuracy of two parts in 10^7. Therefore, the Compton profile for $q > P_{\max}$ is simply defined by the one-dimensional integral Eq. (21) yielding $J_{\mathrm{av}}(q)$ for any scattering direction $\vec{n}$. For $q < P_{\max}$ we divide the $(\tilde{p}_x,\tilde{p}_y)$ plane by a circle of radius $P_{\max}$. The contribution to the integral equation (1) from outside the circle is simply $J_{\mathrm{av}}(\sqrt{q^2+P_{\max}^2})$ since in this region the momentum density is spherical, at least within the accuracy given above. The evaluation of the remaining integral over the interior of the circle is quite tedious as it needs the knowledge of the Bloch functions $|n,\vec{k}\rangle$ with $\vec{k}+\vec{K}=\vec{p}$ on a rather dense two-dimensional grid of $\vec{p}$ vectors. In contrast to this task the effort for the evaluation of the momentum density function $\rho(\vec{p})$ is marginal.[58] A considerable reduction of the numerical work is possible by using a two-dimensional grid of points which were originally proposed to perform Brillouin zone integrals: The momentum space is divided into identical cubes with edges oriented parallel to the cubic [100] axis of length $(1/M)(2\pi/a)$. Their centers of gravity define a simple cubic lattice. For any value of the unit vector $\vec{n}$ normal to a plane characterized by a triple of Miller indices $(m,n,1)$ there exists an orthogonal transformation which carries to the coordinate system $(\tilde{p}_x,\tilde{p}_y,\tilde{p}_z)$ with the consequence that the submanifold of the grid points having the same value $\tilde{p}_z$ form a two-dimensional lattice. For further details we refer to Appendix B where it is shown that the possible values of $\tilde{p}_z$ are discrete and given by

$$q = \frac{1}{\sqrt{m^2+n^2+1}} I_3 \frac{1}{2M} \frac{2\pi}{a}, \tag{25}$$

where $I_3=0,1,\ldots$To comply with recent experiments and the aim to reliably identify fine structures in the profiles we have chosen $M=50$. This gives 5740 $\vec{p}$ points in the irreducible wedge of the Brillouin zone and almost 800 million points lying within the sphere of radius $P_{\max}$. About 1 million two-dimensional $\vec{p}$ points are contained in the circle of radius $P_{\max}$ for $q \leqslant 3.0$ a.u. As shown in Appendix B, the pattern of the two-dimensional grid strongly depends on the Miller indices. In the most general case, also investigated by Schülke *et al.*[1] it is an oblique lattice and the pattern of two neighbored planes differ from one another by a shift of a nonprimitive lattice vector. According to Eq. (25) larger values of m and n imply a shorter distance of neighbored planes which are, on the other side, less densely populated. Finally the integration over the two-dimensional grid is approximated by a scheme[26] similar to that proposed by Gilat and Raubenheimer[52,53] which allows to take into account the exact position of the Fermi break within the corresponding parallelepipeds. To reduce the noise due to the discretization the extension of these parallelepipeds in $\tilde{p}_z$ was chosen finite, but rather small compared to $(1/M)(2\pi/a)$.

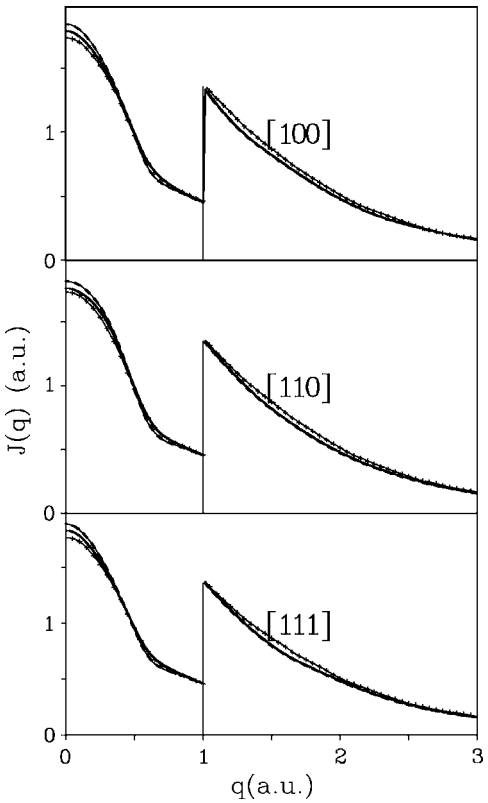

FIG. 7. The all-electron Compton profile along [100], [110], and [111]. Full curves: theoretical result with LP corrections included, dashed curves without LP corrections; both convoluted with a Gaussian with FWHM of 0.18 a.u. Crosses connected by thin curves: experimental results (see Ref. 1). Scale enlarged by factor 3 for $q \geqslant 1.0$ a.u.

B. Comparison with experiments

The Compton profiles of all electrons along the principal directions are displayed in Fig. 7. LP corrections have been included in the full curve. Both theoretical curves are convoluted with a Gaussian with FWHM of 0.18 a.u. according to Schülke.[54] For comparison the corresponding measured CPs are plotted which have slightly been renormalized, mostly by less than 0.5%, according to the theoretical results with LP corrections included. Obviously the LP corrections significantly improve the agreement with the experimental results. Apart from a narrow momentum range where the CPs manifestly vary the LP-corrected theoretical curve and the experimental curves almost merge. This is made more clear in Fig. 8 where the differences between the theoretical and measured profiles along the principal directions are displayed

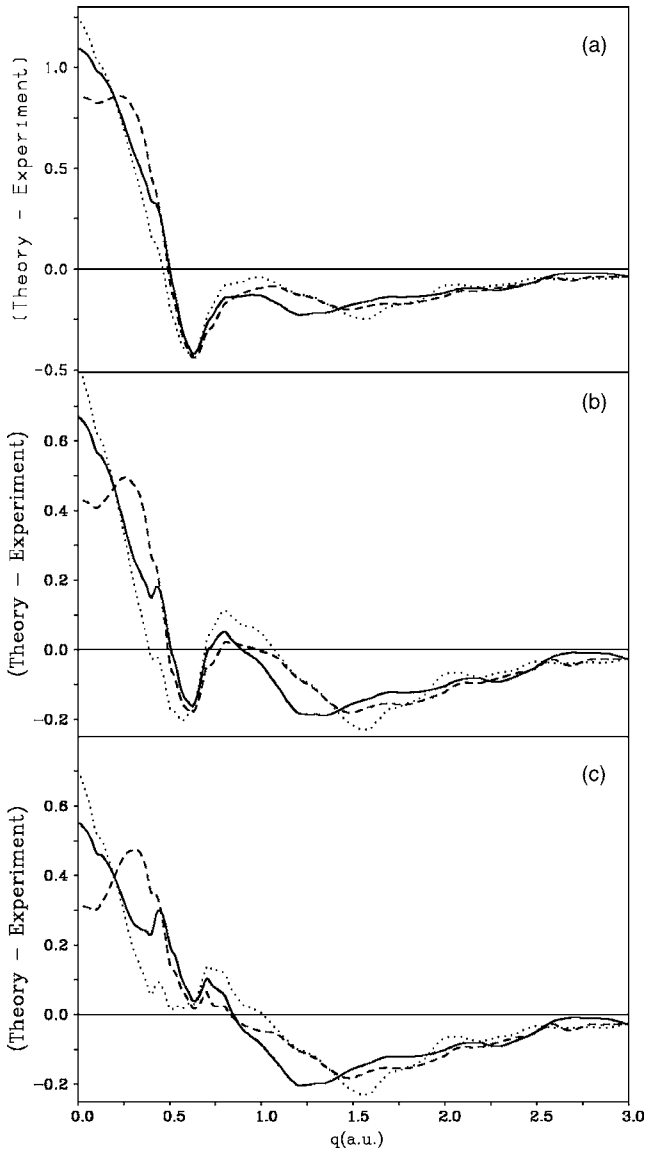

FIG. 8. Differences between the calculated and the experimental valence-electron Compton profiles. (a) LDA results without LP corrections, (b) LP corrections (Ref. 13) included, (c) LP corrections (Ref. 12) included. [100]: full curve, [110]: dashed curve, [111]: dotted curve. Note, that in panels (b) and (c) the scale is enlarged by 1.45. All in units of 0.1 electrons/a.u.

The uncorrected results shown in panel (a) behave quite similarly as the profiles derived with the KKR scheme:[4] at small values of q the theoretical values are overestimated up to 8% and a broad cusp occurs in the opposite direction in the momentum range [0.6,1.2] a.u. As far as comparison is possible the MAPW calculations yield a small improvement of 10%. An essential step in the direction of the experimental results is due to the LP corrections[12,13] as demonstrated by panels (b) and (c). Up to 1.2 a.u. the LP corrections based on the density N_f (Ref. 13) approximately reduce the differences by a factor 1.5. A further improvement is caused by N_f,[12] especially near the cusp structures where the differences are found in the magnitude of the experimental errors. This allows the conclusion that in the case of Li this kind of many-body correction produces significant improvement near the Fermi surface.

TABLE III. Compton profiles along the directions of Ref. 1. Second column: The corresponding weights $g_{\vec{n}}$, third and fourth column: Maximal deviation between theoretical and experimental all-electron Compton profiles $|\delta J|$ in a.u., fifth and sixth column: Square root of the variance in a.u. evaluated in the range $0 \leqslant q \leqslant 1.0$ a.u.

$\vec{n}$	$g_{\vec{n}}$	$\lvert\delta J_{\max}\rvert^{12}$	$\lvert\delta J_{\max}\rvert^{13}$	σ^{12}	σ^{13}
[100]	0.0449234	0.0551	0.0682	0.0270	0.0308
[110]	0.0690973	0.0474	0.0507	0.0266	0.0297
[111]	0.0502865	0.0700	0.0823	0.0273	0.0332
[210]	0.1065961	0.0508	0.0573	0.0294	0.0332
[211]	0.0903624	0.0454	0.0585	0.0222	0.0274
[221]	0.0839212	0.0438	0.0569	0.0207	0.0254
[310]	0.0690797	0.0408	0.0482	0.0256	0.0294
[311]	0.0604653	0.0487	0.0557	0.0294	0.0351
[321]	0.1957635	0.0388	0.0491	0.0233	0.0276
[331]	0.0692293	0.0463	0.0593	0.0271	0.0316
[621]	0.1602754	0.0408	0.0497	0.0236	0.0274
Mean		0.0456	0.0553	0.0251	0.0294

To show more quantitatively the quality of the agreement between theory and experiment for each direction the maximal deviations of the Compton profile $|\delta J|$ and the square root of the variance defined by

$$\sigma = \sqrt{\int_0^{1.0} [J(q) - J_{\exp}(q)]^2 dq} \tag{26}$$

are listed in Table III, using the momentum density functions.[12,13] Except on the [100], [111], and [210] directions the biggest deviations between the experimental and theoretical directional Compton profiles are mostly below $|\delta J| = 0.051$ a.u. The global agreement in the range $0 \leqslant q \leqslant 1.0$ a.u. characterized by the last two columns is at least by a factor 0.54 better. In general the parameterization by Ortiz and Ballone[13] worsens the agreement between theory and experiment in the mean by 12%.

The orientation dependence of the Compton profile is quite small in the case of the free-electron metals like Li. In the case of the data of Schülke *et al.*[1] it can be well described by the coefficients $J_L(q)$ of the expansion in Kubic harmonics which are defined in analogy to Eq. (8) and which are obtained by least-squares fits to the experimental and theoretical profiles along the 11 $\vec{n}$ directions. As already mentioned in Sec. IV the first four coefficients can be considered to be reliable. In Fig. 9 the coefficients J_4, J_6, and J_8 obtained by the MAPW scheme which neither contain core contribution nor are influenced by LP corrections are compared with the experimental values. In addition the result of the Fourier-Hankel reconstruction method based on the expansion of the EMD in Kubic harmonics is displayed after having been folded by a Gaussian with FWHM=0.18 a.u. In contrast to the previous considerations we have evaluated the CP along

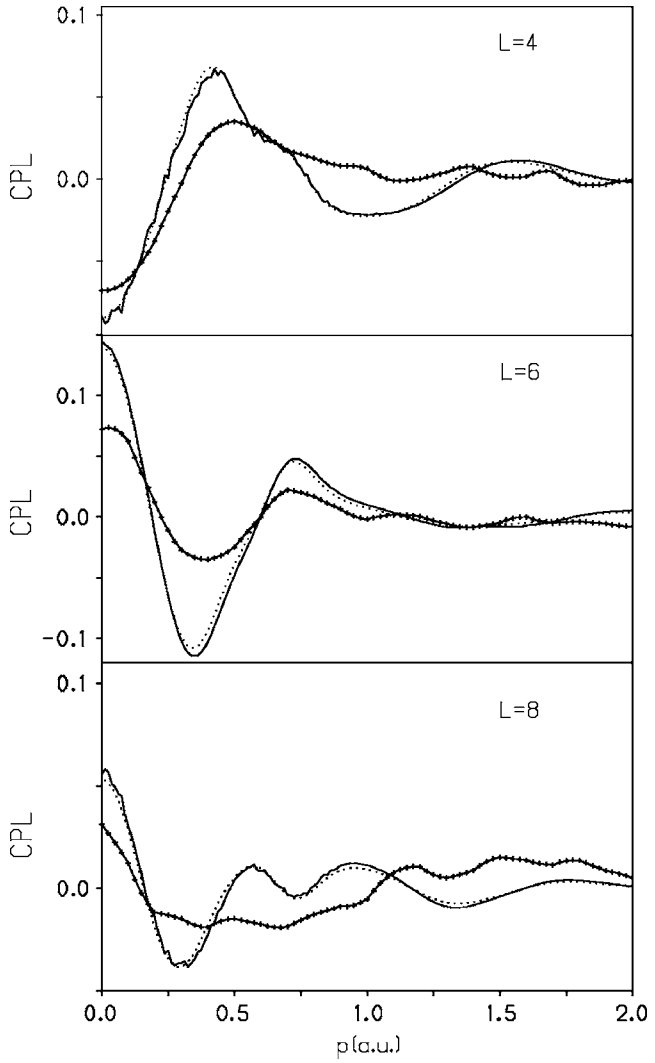

FIG. 9. Expansion of the CPs in terms of KH normalized to 4π on the unit sphere. Full line: MAPW results, dotted line: Fourier-Hankel scheme using theoretical $g_L(q)$ in (10), string of crosses: experimental data. All in units of 0.1 electrons/a.u.

the 24 especially chosen directions (see Sec. V C) by use of Eq. (10). It is remarkable that both theoretical curves almost coincide; obviously the folding procedure has eliminated all features in the Fourier-Hankel curves which are caused by the rapid variation of the EMDs near p_F. In their overall shape they fairly well agree with the experimental results, especially in the case of $L=4$. In view of the smallness of the anisotropy which mostly is comparable with the accuracy of the measurement, not too much significance should be attached to the discrepancies.

Both the first and second derivatives of the profiles $dJ(q)/dq$ and $d^2J(q)/dq^2$ derived by spline interpolation show considerable noise which is completely reduced by convoluting with a Gaussian of FWHM=0.18 a.u. According to Fig. 10 which shows the second derivatives there is good agreement between the theoretical and experimental curves as to both the positions and the heights of the peaks. On both sides of the maxima the theoretical curves smooth the wiggling feature of the experimental CPs within the error

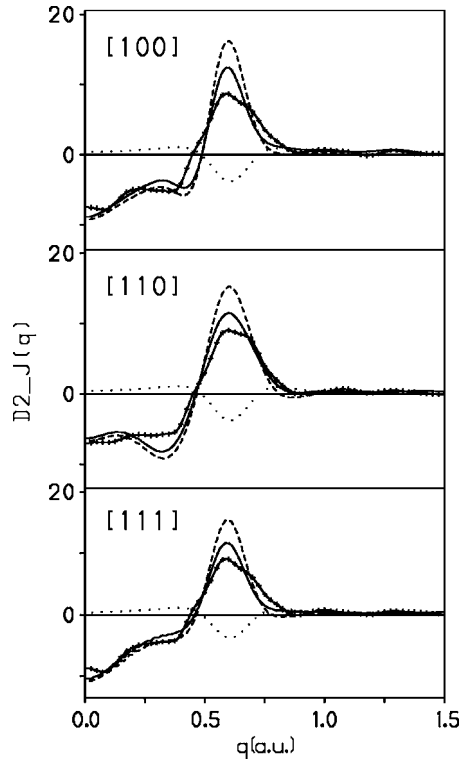

FIG. 10. Second derivatives of the computed and measured profiles. Dashed curve: Valence electron MAPW result, full curve: LP corrections included, string of crosses: experimental data, dotted curve upper panel: LP corrections. Ordinate $d^2J(q)/dq^2$ in units electrons a.u. The maxima of the theoretical curve are approximately located at 0.5995, 0.6036, and 0.5907 a.u. in [100], [110], and [111] direction, respectively.

bars displayed in Fig. 1 of Ref. 50. The width of the experimental maxima are definitely broader than the FWHM =0.18 a.u. with the consequence that the heights are lowered against the theoretical results. In addition, in [100] and [110] an additional shoulder on the high momentum side is visible. Again the LP corrections shift the heights of the maxima in the correct direction but have small influence on their positions. Apart from the fact that the experimental second derivatives have an additional shoulder on the high momentum side the maxima of the theoretical and experimental curves almost coincide but are closer to the spherical average than the diameters listed in Table I, implying a smaller asphericity of the Fermi surface.

To get some insight how a rise of temperature influences the profiles we have also evaluated the CP's along the [110] direction for $a=3.5104$ a.u. ≈ 6.6337 Å corresponding to the lattice constant at room temperature. Thus at least the influence of thermal expansion is taken into account. Similar as in Sternemann *et al.*[55] the temperature differences $[J(q)_{T=20K}-J(q)_{T=293K}]$ in percent of the low-temperature maximum $J(q=0)_{T=20K}$ are presented in Fig. 11. In addition, the differences of the CPs calculated with the corresponding SCF-MAPW density analogous to Eq. (24) are also plotted. For comparison the experimental differences by Sternemann are shown which, however, are obtained with the low temperature 95 K. Since the lattice constants at 20 and 95 K are

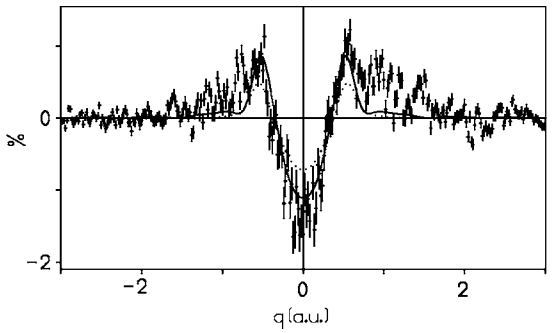

FIG. 11. Experimental CP temperature differences (Ref. 55) $[J(q)_{T=95K}-J(q)_{T=295K}]/J(0)_{T=95K}$, marked by crosses, compared with MAPW differences (full line) and LDA differences (dashed-dotted) line LDA differences using the spatial density for the lower temperature $T=20$ K.

slightly different this change of the low temperature has marginally influence on the theoretical curves. It is remarkable how the theoretical curves follow the experimental results although the coherent scattering of the conduction electrons by the lattice waves is neglected. From these results we learn that a raise of the temperature from 20 to 293 K will increase the CPs by 1% at low momenta and reduce them by 0.8% near k_F. Almost no change of the profiles occurs at higher values of q. These temperature-driven shifts slightly worsen the results shown in Fig. 8, especially near $q=0$.

VII. CONCLUDING REMARKS

The LP corrections of the Compton profile based on the result of recent quantum Monte Carlo simulations differ from one another by up to 18% but are peaked in the same momentum range. It should be a challenge for future theoretical investigations to determine the momentum density function of a Fermi liquid at metallic densities more precisely.

The spherical average of the momentum density found by applying the well-known reconstruction schemes to the experimental data shows little similarity to the theoretical results, especially in the region of the Fermi breaks. For metals only the Fourier-Bessel scheme reliably describes the orientational anisotropy but its results are distinctly smaller than those predicted by theory.

As the Fourier-Hankel scheme followed by folding with an appropriately chosen Gaussian yields reasonably reliable results this procedure can be used in future calculations instead of the two-dimensional integration (1) which is quite CPU expensive.

Similar as in the case of Al we find that a crude picture of the spherically averaged EMD and CP may already be obtained in LDA by use of the momentum density of a Fermi liquid and the nontruncated charge density of a SCF calculation. Again the LP corrections evaluated with this charge density yields the CPs in a wide momentum range in close agreement with the experimental data. The maxima in the second derivatives of the experimental and theoretical profiles imply a smaller asphericity of the Fermi surface than the original band structure calculations suggest.

ACKNOWLEDGMENTS

The author would like to thank Professor W. Schülke for providing results of his high-resolution Compton-scattering study and for fruitful remarks. Stimulating discussions with Professor F. Bell are appreciated. Dr. R. Bader, LRZ München, and Dr. H. Stöhr have critically read the manuscript. The generous hospitality of Professor J. van Delft is gratefully acknowledged.

APPENDIX A: THE SPHERICAL AVERAGE OF THE COMPTON PROFILE

Starting from the definition

$$J_n(q)=\int_\infty\int_\infty\int_\infty \rho(\vec{p})\,\delta(\vec{p}\cdot\vec{n}-q)d^3p, \tag{A1}$$

where δ denotes the Dirac δ function the spherical average $J_{\mathrm{av}}(q)=\int_{[1]}J_n(q)d\Omega$ is evaluated by changing the order of integration. $[1]$ denotes the unit sphere. Then the unit vector $\vec{n}$ is expressed in spherical coordinates ϑ, ϕ with the z axis parallel to $\vec{p}$. This gives

$$J_{\mathrm{av}}(q)=\int_\infty\int_\infty\int_\infty \rho(\vec{p}) \tag{A2}$$

$$\left[\int_0^\pi\int_0^{2\pi}\delta(p\cos\vartheta-q)\sin\vartheta d\vartheta d\phi\right]d^3p.$$

Note that the inner integrand is independent from ϕ whereas the integration over θ yields the Heaviside step function Θ,

$$J_{\mathrm{av}}(q)=2\pi\int_\infty\int_\infty\int_\infty\frac{1}{p}\rho(\vec{p})\Theta(p-q)d^3p. \tag{A3}$$

Finally, in spherical polar coordinate the two-dimensional integral over the unit sphere gives the spherical average $\rho_{\mathrm{av}}(p)$,

$$J_{\mathrm{av}}(q)=2\pi\int_q^\infty\rho_{\mathrm{av}}(p)pdp. \tag{A4}$$

In summary the spherical average of the CP is uniquely determined by the spherical average of the EMD.

APPENDIX B: THE TWO-DIMENSIONAL GRID IN THE CASE OF THE MILLER INDICES (m, n,1)

The orthogonal transformation with the matrix

$$\boldsymbol{\alpha}=\begin{pmatrix}\frac{-n}{R_1} & \frac{m}{R_1} & 0\\ \frac{m}{R_2} & \frac{n}{R_2} & \frac{-m^2-n^2}{R_2}\\ \frac{m}{R_3} & \frac{n}{R_3} & \frac{1}{R_3}\end{pmatrix}, \tag{B1}$$

where $R_1^2=m^2+n^2$, $R_2^2=m^2+n^2-(m^2+n^2)^2$, $R_3^2=1+m^2+n^2$ carries from the original Cartesian coordinate frame to the

coordinates p_x', p_y', p_z' with the p_z' axis in the direction of $\vec{n}$. In this system the vectors pointing to the centers of gravity of the cubes obtained by subdividing the whole $\vec{p}$ space have the components characterized by the integers (i,j,k):

$$p_x' = [-n(2i-1) + m(2j-1)]/R_1 \frac{1}{2M}\frac{2\pi}{a}, \tag{B2}$$

$$p_y' = [m(2i-1) + n(2j-1) - (m^2+n^2)(2k-1)]/R_2 \frac{1}{2M}\frac{2\pi}{a}, \tag{B3}$$

$$p_z' = [m(2i-1) + n(2j-1) + (2k-1)]/R_3 \frac{1}{2M}\frac{2\pi}{a}. \tag{B4}$$

With the new integer

$$I_3 = m(2i-1) + n(2j-1) + (2k-1) \tag{B5}$$

we get

$$q = p_z' = \frac{1}{2MR_3}\frac{2\pi}{a} I_3. \tag{B6}$$

After elimination of the integer k by use of Eq. (B5) we note that the two-dimensional vectors with components p_x', p_y' may be expressed by

$$\vec{p}' = \left[\frac{2i-1}{2} - \frac{m(m^2+n^2)}{2(1+m^2+n^2)^2} I_3\right]\vec{a}_1' + \left[\frac{2j-1}{2} - \frac{n(m^2+n^2)}{2(1+m^2+n^2)^2} I_3\right]\vec{a}_2' \tag{B7}$$

by use of the following two-dimensional basis vectors

$$\vec{a}_1' = [-2n/R_1, 2m(1+m^2+n^2)/R_2]\frac{1}{2M}\frac{2\pi}{a}, \tag{B8}$$

$$\vec{a}_2' = [2m/R_1, 2n(1+m^2+n^2)/R_2]\frac{1}{2M}\frac{2\pi}{a}. \tag{B9}$$

Thus we learn, that the points of the two-dimensional grid suffer a nonprimitive translation with any change of the integer I_3. This pattern repeats after I_3 has changed by the value $2(1+m^2+n^2)$.

APPENDIX C: INTERPOLATION OF THE EXPERIMENTAL PROFILES

To get a more dense set of scattering directions $\vec{n}$ without producing spurious oscillations the following scheme is produced. For a given directions $\vec{n}_j$ on the unit sphere the next three directions of the experimental profiles are searched for. With the direction $\vec{n}_j$ as axis of local spherical coordinates ϑ, ϕ we assume the interpolation function

$$f = a + b \sin\vartheta\cos\phi + c \sin\vartheta \sin\phi, \tag{C1}$$

where the coefficients a, b, and c are determined by the magnitudes of the $J_{\vec{n}}(q)$ on the next three directions. Then $J_{\vec{n}_j}(q) = a$.

[1] W. Schülke, G. Stutz, F. Wohlert, and A. Kaprolat, Phys. Rev. B **54**, 14381 (1996).
[2] LDA calculations by A. Bansil and S. Kaprzyk, Department of Physics, Northwestern University, Boston, MA.
[3] L. Lam and P. M. Platzman, Phys. Rev. B **9**, 5122 (1974).
[4] Y. Sakurai, Y. Tanaka, A. Bansil, S. Kaprzyk, A. T. Stewart, Y. Nagashima, T. Hyodo, S. Nanao, H. Kawata, and N. Shiotani, Phys. Rev. Lett. **74**, 2252 (1995).
[5] T. Baruah, R. R. Zope, and A. Kshirsagar, Phys. Rev. B **60**, 10770 (1999).
[6] H. Bross, J. Phys.: Condens. Matter **16**, 7363 (2004).
[7] H. Bross, G. Bohn, G. Meister, W. Schubö, and H. Stöhr, Phys. Rev. B **2**, 3098 (1970).
[8] S. H. Vosko, L. Wilk, and M. Nusair, Can. J. Phys. **58**, 1200 (1980)
[9] J. P. Perdew, Phys. Rev. B **33**, 8822 (1986); **34**, 7406 (1986).
[10] J. P. Perdew, J. A. Chevary, S. H. Vosko, K. A. Jackson, M. R. Pederson, D. J. Singh, and C. Fiolhais, Phys. Rev. B **46**, 6671 (1992).
[11] J. P. Perdew, K. Burke, and M. Ernzerhof, Phys. Rev. Lett. **77**, 3865 (1996).
[12] B. Farid, V. Heine, G. E. Engel, and I. J. Robertson, Phys. Rev. B **48**, 11602 (1993).
[13] G. Ortiz and P. Ballone, Phys. Rev. B **50**, 1391 (1994).
[14] P. E. Mijnarends, in *Compton Scattering*, edited by B. G. Williams(McGraw-Hill, New York, 1977), p. 323.
[15] P. E. Mijnarends, Phys. Rev. **160**, 512 (1967).
[16] N. K. Hansen, *Reconstruction of the EMD from a Set of Directional Compton Profiles* (Hahn Meitner Institute, Berlin, 1980), Rep. HMI B 342.
[17] H. Roth-Seefried and H. Bross, Z. Phys. B **26**, 125 (1977).
[18] H. Bross, Eur. Phys. J. B **37**, 405 (2004).
[19] A. Bansil, Solid State Commun. **16**, 885 (1975).
[20] W. R. Fehlner and S. H. Vosko, Can. J. Phys. **54**, 2159 (1976).
[21] W. R. Fehlner, S. B. Nickerson, and S. H. Vosko, Solid State Commun. **19**, 83 (1976).
[22] R. Prasad and A. Bansil, Phys. Rev. B **21**, 496 (1980).
[23] H. Bross (unpublished).
[24] D. J. Chadi and M. L. Cohen, Phys. Rev. B **8**, 5747 (1973).
[25] H. J. Monkhorst and J. D. Pack, Phys. Rev. B **13**, 5188 (1976).
[26] H. Bross, J. Phys. F: Met. Phys. **8**, 2631 (1978).
[27] P. Dufek, P. Blaha, and K. Schwarz, Phys. Rev. B **50**, 7279, (1994).
[28] J. E. Jaffe, Z. Lin, and A. C. Hess, Phys. Rev. B **57**, 11834 (1998).
[29] R. Berliner and S. A. Werner, Phys. Rev. B **34**, 3586 (1986).
[30] H. G. Smith, Phys. Rev. Lett. **58**, 1228 (1987).
[31] D. L. Randles and M. Springford, J. Phys. F: Met. Phys. **6**, 1827

(1976).
[32] *Landolt-Börnstein* (Springer, Berlin, 1984), Vol. 13c, p. 203.
[33] U. von Barth and L. Hedin, J. Phys. C **5**, 1629 (1972).
[34] M. Rasolt, S. B. Nickerson, and S. H. Vosko, Solid State Commun. **16**, 827 (1975).
[35] A. H. MacDonald, J. Phys. F: Met. Phys. **10**, 1737 (1980).
[36] H. Bross, Phys. Status Solidi B **229**, 1359 (2002).
[37] Y. Tanaka, Y. Sakurai, A. T. Stewart, N. Shiotani, P. E. Mijnarends, S. Kaprzyk, and A. Bansil, Phys. Rev. B **63**, 045120 (2001).
[38] C. Filippi and D. M. Ceperley, Phys. Rev. B **59**, 7907 (1999).
[39] P. Rennert, Phys. Status Solidi B **105**, 567 (1981).
[40] D. A. Cardwell and M. J. Cooper, J. Phys.: Condens. Matter **1**, 9357 (1989).
[41] B. I. Lundqvist, Phys. Kondens. Mater. **6**, 193 (1967); **6**, 206 (1967); **7**, 117 (1968).
[42] D. M. Ceperley and B. J. Alder, Phys. Rev. Lett. **45**, 566 (1980).
[43] B. Barbiellini and A. Bansil, J. Phys. Chem. Solids **62**, 2181 (2001).
[44] Y. Yasuhara and Y. Kawazoe, Physica A **85**, 416 (1976).
[45] A. W. Overhauser, Can. J. Phys. **73**, 683 (1995).
[46] V. L. Moruzzi, J. F. Janak, and A. R. Williams, *Calculated Electronic Properties of Metals* (Pergamon Press, New York, 1978).
[47] P. Pattison, W. Weyrich, and B. G. Williams, Solid State Commun. **21**, 967 (1977).
[48] F. Biggs, L. B. Mendelsohn, and J. B. Mann, At. Data Nucl. Data Tables **16**, 201 (1975).
[49] Y. Tanaka, Y. Sakurai, A. T. Stewart, N. Shiotani, P. E. Mijnarends, S. Kaprzyk, and A. Bansil Phys. Rev. B **63**, 045120 (2000).
[50] T. Ohata, M. Itou, I. Matsumoto, Y. Sakurai, H. Kawata, N. Shiotani, S. Kaprzyk, P. E. Mijnarends, and A. Bansil, Phys. Rev. B **62**, 16528 (2000).
[51] C. J. Bradley and A. P. Cracknell, *The Mathematical Theory of Symmetry in Solids* (Clarendon Press, Oxford, 1972), Table II.
[52] G. Gilat and L. H. Raubenheimer, Phys. Rev. **144**, 390 (1966).
[53] L. H. Raubenheimer and G. Gilat, Phys. Rev. **157**, 586 (1967).
[54] W. Schülke after having reanalyzed the former data (see Ref. 1) (private communication).
[55] C. Sternemann, T. Buslaps, A. Shukla, P. Suortti, G. Döring, and W. Schülke, Phys. Rev. B **63**, 094301 (2001).
[56] The parameterization as originally proposed in Ref. 43 increases the LP corrections by up to 4% on the low momentum side and has the opposite effect at high momenta.
[57] The weights $g_{\vec{n}}$ are obtained by subdividing the unit sphere in small areas and by assigning each area to one of the 11 directions according to the mutual distance.
[58] In the case of MAPW the relation of the times needed to evaluate the Bloch function and to evaluate its Fourier transform is 30:1.